

Article

Bound States and Supercriticality in Graphene-Based Topological Insulators

Denis Klöpfer¹, Alessandro De Martino² and Reinhold Egger^{1,*}¹ Institut für Theoretische Physik, Heinrich-Heine-Universität, D-40225 Düsseldorf, Germany² Department of Mathematical Science, City University London, London EC1V 0HB, United Kingdom* Author to whom correspondence should be addressed; Email: egger@thphy.uni-duesseldorf.de, Tel. (49) 211 81-14710, Fax (49) 211 81-15630.*Version March 1, 2022 submitted to Crystals. Typeset by L^AT_EX using class file mdpi.cls*

Abstract: We study the bound state spectrum and the conditions for entering a supercritical regime in graphene with strong intrinsic and Rashba spin-orbit interactions within the topological insulator phase. Explicit results are provided for a disk-shaped potential well and for the Coulomb center problem.

Keywords: graphene; supercriticality; spin-orbit interaction

1. Introduction

The electronic properties of graphene monolayers are presently under intense study. Previous works have already revealed many novel and fundamental insights; for reviews, see [1,2]. Following the seminal work of Kane and Mele [3], it may be possible to engineer a two-dimensional (2D) topological insulator (TI) phase [4] in graphene by enhancing the — usually very weak [5–7] — spin-orbit interaction (SOI) in graphene. This enhancement could, for instance, be achieved by the deposition of suitable adatoms [8]. Remarkably, random deposition should already be sufficient to reach the TI phase [9–11] where the effective “intrinsic” SOI Δ exceeds (half of) the “Rashba” SOI λ . So far, the only 2D TIs realized experimentally are based on the mercury telluride class. Using graphene as a TI material constitutes a very attractive option because of the ready availability of high-quality graphene samples [1] and the exciting prospects for stable and robust TI-based devices [4], see also [12,13]

In this work, we study bound-state solutions and the conditions for supercriticality in a graphene-based TI. Such questions can arise in the presence of an electrostatically generated potential well

19 (“quantum dot”) or for a Coulomb center. The latter case can be realized by artificial alignment of
 20 Co trimers [14], or when defects or charged impurities reside in the graphene layer. Without SOI, the
 21 Coulomb impurity problem in graphene has been theoretically studied in depth [15–20]; for reviews, see
 22 [1,2]. Moreover, for $\lambda = 0$, an additional mass term in the Hamiltonian corresponds to the intrinsic
 23 SOI Δ (see below), and the massive Coulomb impurity problem in graphene has been analyzed in
 24 [21–26]. However, a finite Rashba SOI λ is inevitable in practice and has profound consequences. In
 25 particular, $\lambda \neq 0$ breaks electron-hole symmetry and modifies the structure of the vacuum. We therefore
 26 address the general case with both Δ and λ finite, but within the TI phase $\Delta > \lambda/2$, in this paper.
 27 Experimental progress on the observation of Dirac quasiparticles near a Coulomb impurity in graphene
 28 was also reported very recently [14], and we are confident that the topological version with enhanced
 29 SOI can be studied experimentally in the near future. Our work may also be helpful in the understanding
 30 of spin-orbit mediated spin relaxation in graphene [27].

31 The atomic collapse problem for Dirac fermions in an attractive Coulomb potential, $V(r) =$
 32 $-\hbar v_F \alpha / r$, could thereby be realized in topological graphene. Here we use the dimensionless impurity
 33 strength

$$\alpha = \frac{Ze^2}{\kappa \hbar v_F} \simeq 2.2 \frac{Z}{\kappa}, \quad (1)$$

34 where Z is the number of positive charges held by the impurity, κ a dielectric constant characterizing
 35 the environment, and $v_F \approx 10^6$ m/s the Fermi velocity. Without SOI, the Hamiltonian is not self-adjoint
 36 for $\alpha > \alpha_c = 1/2$, and the potential needs short-distance regularization, e.g., by setting $V(r < R) =$
 37 $-\hbar v_F \alpha / R$ with short-distance cutoff R of the order of the lattice constant of graphene [1,2]. Including
 38 a finite “mass” Δ , i.e., the intrinsic SOI, but keeping $\lambda = 0$, the critical coupling α_c is shifted to [24]

$$\alpha_c \simeq \frac{1}{2} + \frac{\pi^2}{\ln^2(0.21 \Delta R / \hbar v_F)}, \quad (2)$$

39 approaching the value $\alpha_c = 1/2$ for $R \rightarrow 0$. In the supercritical regime $\alpha > \alpha_c$, the lowest bound state
 40 “dives” into the valence band continuum (Dirac sea). It then becomes a resonance with complex energy,
 41 where the imaginary part corresponds to the finite decay rate into the continuum. Below we show that
 42 the Rashba SOI provides an interesting twist to this supercriticality story.

43 The structure of this article is as follows. In Sec. 2 we introduce the model and summarize its
 44 symmetries. The case of a circular potential well is addressed in Sec. 3 before turning to the Coulomb
 45 center in Sec. 4. Some conclusions are offered in Sec. 5. Note that we do not include a magnetic field
 46 (see, e.g., [28,29]) and thus our model enjoys time-reversal symmetry. Below, we often use units with
 47 $\hbar = v_F = 1$.

48 2. Model and symmetries

49 2.1. Kane-Mele model with radially symmetric potential

50 We study the Kane-Mele model for a 2D graphene monolayer with both intrinsic (Δ) and Rashba (λ)
 51 SOI [3] in the presence of a radially symmetric scalar potential $V(r)$. Assuming that $V(r)$ is sufficiently

smooth to allow for the neglect of inter-valley scattering, the low-energy Hamiltonian near the K point ($\tau = +1$) is given by

$$H = \tau\sigma_x p_x + \sigma_y p_y + \tau\Delta\sigma_z s_z + \frac{\lambda}{2}(\tau\sigma_x s_y - \sigma_y s_x) + V(r), \quad (3)$$

with Pauli matrices $\sigma_{x,y,z}$ ($s_{x,y,z}$) in sublattice (spin) space [1]. The Hamiltonian near the other valley (K' point) follows for $\tau = -1$ in Eq. (3). We note that a sign change of the Rashba SOI, $\lambda \rightarrow -\lambda$, does not affect the spectrum due to the relation $H(-\lambda) = s_z H(\lambda) s_z$. Without loss of generality, we then put $\Delta \geq 0$ and $\lambda \geq 0$.

Using polar coordinates, it is now straightforward to verify (see also [21]) that total angular momentum, defined as

$$J_z = -i\partial_\phi + s_z/2 + \tau\sigma_z/2, \quad (4)$$

is conserved and has integer eigenvalues j . For given j , eigenfunctions of H must then be of the form

$$\Psi_{j,\tau=\pm}(r, \phi) = \begin{pmatrix} e^{i(j-1)\phi} a_{\uparrow,j,+}(r) \\ ie^{ij\phi} b_{\uparrow,j,+}(r) \\ e^{ij\phi} a_{\downarrow,j,+}(r) \\ ie^{i(j+1)\phi} b_{\downarrow,j,+}(r) \end{pmatrix}, \quad \Psi_{j,-}(r, \phi) = \begin{pmatrix} e^{ij\phi} a_{\uparrow,j,-}(r) \\ ie^{i(j-1)\phi} b_{\uparrow,j,-}(r) \\ e^{i(j+1)\phi} a_{\downarrow,j,-}(r) \\ ie^{ij\phi} b_{\downarrow,j,-}(r) \end{pmatrix}. \quad (5)$$

Next we combine the radial functions to (normalized) four-spinors,

$$\Phi_{j,\tau}(r) = \begin{pmatrix} a_{\uparrow,j,\tau}(r) \\ b_{\uparrow,j,\tau}(r) \\ a_{\downarrow,j,\tau}(r) \\ b_{\downarrow,j,\tau}(r) \end{pmatrix}. \quad (6)$$

In this representation, the radial Dirac equation for total angular momentum j and valley index $\tau = \pm$ reads

$$(H_{j,\tau} - E) \Phi_{j,\tau}(r) = 0, \quad (7)$$

with Hermitian matrix operators (note that Δ denotes the intrinsic SOI and not the Laplacian)

$$H_{j,+} = \begin{pmatrix} \Delta + V & \nabla_j^{(+)} & 0 & 0 \\ \nabla_{j-1}^{(-)} & -\Delta + V & -\lambda & 0 \\ 0 & -\lambda & -\Delta + V & \nabla_{j+1}^{(+)} \\ 0 & 0 & \nabla_j^{(-)} & \Delta + V \end{pmatrix}, \quad (8)$$

$$H_{j,-} = \begin{pmatrix} -\Delta + V & \nabla_{j-1}^{(-)} & 0 & -\lambda \\ \nabla_j^{(+)} & \Delta + V & 0 & 0 \\ 0 & 0 & \Delta + V & \nabla_j^{(-)} \\ -\lambda & 0 & \nabla_{j+1}^{(+)} & -\Delta + V \end{pmatrix},$$

where we use the notation

$$\nabla_j^{(\pm)} = \frac{j}{r} \pm \frac{d}{dr}. \quad (9)$$

One easily checks that Eq. (8) satisfies the parity symmetry relation

$$H_{-j,\tau} = \sigma_y s_y H_{j,\tau} \sigma_y s_y. \quad (10)$$

67 Note that this ‘‘parity’’ operation for the radial Hamiltonian is non-standard in the sense that the valley
 68 is not changed by the transformation $\sigma_y s_y$, spin and sublattice are flipped simultaneously, and only the
 69 y -coordinate is reversed. (We will nonetheless refer to $\sigma_y s_y$ as parity transformation below.) A second
 70 symmetry relation connects both valleys,

$$H_{j,-\tau} = \sigma_x H_{j,\tau} \sigma_x. \quad (11)$$

71 Using Eq. (10), this relation can be traced back to a time-reversal operation. Equations (10) and (11)
 72 suggest that eigenenergies typically are four-fold degenerate.

73 When projected to the subspace of fixed (integer) total angular momentum j , the current density
 74 operator has angular component $J_\phi = \sigma_x$ and radial component $J_r = -\tau \sigma_y$ for arbitrary j . When
 75 real-valued entries can be chosen in $\Phi_{j,\tau}(r)$, the radial current density thus vanishes separately in each
 76 valley. We define the (angular) spin current density as $J_\phi^S = s_z \sigma_x$. Remarkably, the transformation
 77 defined in Eq. (11) conserves both (total and spin) angular currents, while the transformation in Eq. (10)
 78 reverses the total current but conserves the spin current. Therefore, at any energy, eigenstates supporting
 79 spin-filtered counterpropagating currents are possible. However, in contrast to the edge states found in a
 80 ribbon geometry [3], these spin-filtered states do not necessarily have a topological origin.

81 We focus on one K point ($\tau = +$) and omit the τ -index henceforth; the degenerate $\tau = -$ Kramers
 82 partner easily follows using Eq. (11). In addition, using the symmetry (10), it is sufficient to study the
 83 model for fixed total angular momentum $j \geq 0$.

84 2.2. Zero total angular momentum

85 For arbitrary $V(r)$, we now show that a drastic simplification is possible for total angular momentum
 86 $j = 0$, which can even allow for an exact solution. Although the lowest-lying bound states for the
 87 potentials in Secs. 3 and 4 are found in the $j = 1$ sector, exact statements about what happens for $j = 0$
 88 are valuable and can be explored along the route sketched here.

89 The reason why $j = 0$ is special can be seen from the parity symmetry relation in Eq. (10). The parity
 90 transformation $\sigma_y s_y$ connects the $\pm j$ sectors, but represents a discrete symmetry of the $j = 0$ radial
 91 Hamiltonian $H_{j=0,\tau}$ [see Eq. (8)] acting on the four-spinors in Eq. (6). Therefore, the $j = 0$ subspace
 92 can be decomposed into two orthogonal subspaces corresponding to the two distinct eigenvalues of the
 93 Hermitian operator $\sigma_y s_y$. This operator is diagonalized by the matrix

$$U = \frac{1}{\sqrt{2}} \begin{pmatrix} 1 & 0 & 0 & -1 \\ 0 & 1 & 1 & 0 \\ 1 & 0 & 0 & 1 \\ 0 & 1 & -1 & 0 \end{pmatrix}, \quad (12)$$

94 such that

$$U \sigma_y s_y U^{-1} = \text{diag}(1, 1, -1, -1). \quad (13)$$

95 In fact, using this transformation matrix to carry out a similarity transformation, $\tilde{H}_{j,+} = UH_{j,+}U^{-1}$, we
96 obtain

$$\tilde{H}_{j,+} = \begin{pmatrix} \Delta + V & \partial_r & 0 & j/r \\ -1/r - \partial_r & -\Delta + V - \lambda & j/r & 0 \\ 0 & j/r & \Delta + V & \partial_r \\ j/r & 0 & -1/r - \partial_r & -\Delta + \lambda + V \end{pmatrix}. \quad (14)$$

97 For $j = 0$, the upper and lower 2×2 blocks decouple. Each block has the signature (“parity”) $\sigma = \pm$
98 corresponding to the eigenvalues in Eq. (13), and represents a mixed sublattice-spin state, see Eqs. (6)
99 and (12).

100 For parity $\sigma = \pm$, the 2×2 block matrix in Eq. (14) is formally identical to an effective $\lambda = 0$
101 problem with $j = 0$, fixed $s_z = \sigma$, and the substitutions

$$\Delta \rightarrow \Delta + \sigma\lambda/2, \quad E \rightarrow E + \sigma\lambda/2. \quad (15)$$

102 This implies that for $j = 0$ and arbitrary $V(r)$, the complete spectral information for the full Kane-Mele
103 problem (with $\lambda \neq 0$) directly follows from the $\lambda = 0$ solution.

104 2.3. Solution in region with constant potential

105 We start our analysis of the Hamiltonian (3) with the general solution of Eq. (7) for a region of constant
106 potential. Here, it suffices to study $V(r) = 0$, since E and V enter only through the combination $E - V$
107 in Eq. (8). In Sec. 3, we will use this solution to solve the case of a step potential.

108 The general solution to Eq. (7) follows from the Ansatz

$$\Phi_j(r) = \begin{pmatrix} c_1 B_{j-1}(\sqrt{p}r) \\ c_2 B_j(\sqrt{p}r) \\ c_3 B_j(\sqrt{p}r) \\ c_4 B_{j+1}(\sqrt{p}r) \end{pmatrix}. \quad (16)$$

109 where the c_i are real coefficients, B_j is one of the cylinder (Bessel) functions, $B_j = J_j$ or $B_j = H_j^{(1)}$,
110 and p denotes a real spectral parameter. In particular, \sqrt{p} is a generalized radial wavenumber. We here
111 assume true bound-state solutions with real-valued energy. However, for quasi-stationary resonance
112 states with complex energy, p and the c_i may be complex as well.

113 Using the Bessel function recurrence relation, $\nabla_j^{(\pm)} B_j(\sqrt{p}r) = \sqrt{p} B_{j\mp 1}(\sqrt{p}r)$, the set of four coupled
114 differential equations (7) simplifies to a set of algebraic equations,

$$\begin{pmatrix} \Delta - E & \sqrt{p} & 0 & 0 \\ \sqrt{p} & -\Delta - E & -\lambda & 0 \\ 0 & -\lambda & -\Delta - E & \sqrt{p} \\ 0 & 0 & \sqrt{p} & \Delta - E \end{pmatrix} \begin{pmatrix} c_1 \\ c_2 \\ c_3 \\ c_4 \end{pmatrix} = 0. \quad (17)$$

115 Notably, j does not appear here, and therefore the spectral parameter p depends only on the energy E .
116 The condition of vanishing determinant then yields a quadratic equation for p , with the two solutions

$$p_{\pm} = (E - \Delta)(E - E_{\pm}), \quad E_{\pm} = -\Delta \pm \lambda. \quad (18)$$

117 Which Bessel function is chosen in Eq. (16) now depends on the sign of p_{\pm} and on the imposed regularity
 118 conditions for $r \rightarrow 0$ and/or $r \rightarrow \infty$.

119 For $p_{\pm} > 0$, a solution regular at the origin is obtained by putting $B_j = J_j$, which describes standing
 120 radial waves. Equation (17) then yields the unnormalized spinor

$$\Phi_{j,p_{\pm}>0}(r) = \begin{pmatrix} \frac{\sqrt{p_{\pm}}}{E-\Delta} J_{j-1}(\sqrt{p_{\pm}}r) \\ J_j(\sqrt{p_{\pm}}r) \\ \mp J_j(\sqrt{p_{\pm}}r) \\ \mp \frac{\sqrt{p_{\pm}}}{E-\Delta} J_{j+1}(\sqrt{p_{\pm}}r) \end{pmatrix}. \quad (19)$$

121 For $p_{\pm} < 0$, instead it is convenient to set $B_j = H_j^{(1)}$ in Eq. (16). Using the identity $H_j^{(1)}(ze^{i\pi/2}) =$
 122 $\frac{2}{\pi i} e^{-ij\pi/2} K_j(z)$, the unnormalized spinor resulting from Eq. (17) then takes the form

$$\Phi_{j,p_{\pm}<0}(r) = \begin{pmatrix} -\frac{\sqrt{-p_{\pm}}}{E-\Delta} K_{j-1}(\sqrt{-p_{\pm}}r) \\ K_j(\sqrt{-p_{\pm}}r) \\ \mp K_j(\sqrt{-p_{\pm}}r) \\ \mp \frac{\sqrt{-p_{\pm}}}{E-\Delta} K_{j+1}(\sqrt{-p_{\pm}}r) \end{pmatrix}, \quad (20)$$

123 where the modified Bessel function $K_j(\sqrt{-p_{\pm}}r)$ describes evanescent modes, exponentially decaying at
 124 infinity.

125 2.4. Solution without potential

126 In a free system, i.e., when $V(r) = 0$ for all r , the only acceptable solution corresponding to a physical
 127 state is obtained when $p_{\pm} > 0$ [30]. For $\Delta < \lambda/2$, at least one $p_{\pm} > 0$ in Eq. (18) for all E , and the
 128 system is gapless. However, the TI phase defined by $\Delta > \lambda/2$ has a gap as we show now.

129 For $\Delta > \lambda/2$, Eq. (18) tells us that for $E > \Delta$ and for $E < E_-$, both solutions p_{\pm} are positive and
 130 hence (for given j and τ) there are two eigenstates $\Phi_{j,p_{\pm}}$ for given energy E . However, within the energy
 131 window [with E_{\pm} in Eq. (18)]

$$E_- < E < E_+, \quad (21)$$

132 we have $p_+ > 0$ and $p_- < 0$, i.e., only the eigenstate Φ_{j,p_+} represents a physical solution. Both p_{\pm}
 133 are negative when $E_+ < E < \Delta$, and no physical state exists at all. This precisely corresponds to
 134 the topological gap in the TI phase [3]. Note that due to the Rashba SOI, the valence band edge is
 135 characterized by the two energies E_{\pm} , with halved density of states in the energy window (21). One
 136 may then ask at which energy (E_+ or E_-) the supercritical diving of a bound state level in an impurity
 137 potential takes place.

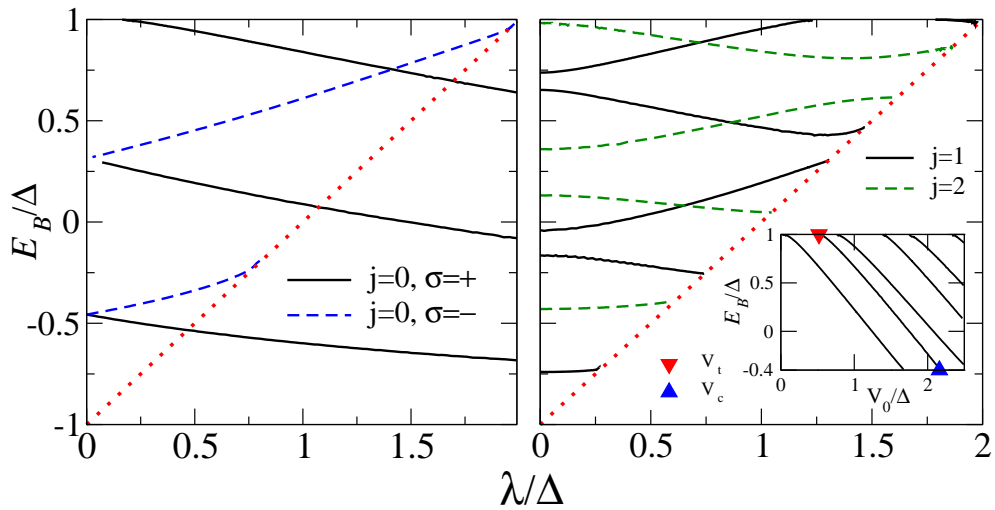
138 3. Circular potential well

139 3.1. Bound states

140 In this section, we study a circular potential well with radius R and depth $V_0 > 0$,

$$V(r) = \begin{cases} -V_0, & r < R \\ 0, & r \geq R \end{cases} \quad (22)$$

Figure 1. Bound-state spectrum (E_B) vs Rashba SOI (λ) for a circular potential well with depth $V_0 = 2\Delta$ and radius $R = 3/\Delta$. Only the lowest-energy states with $j = 0, 1, 2$ are shown. The red dotted line indicates $E_+ = -\Delta + \lambda$. The left panel shows $j = 0$ bound states with parity $\sigma = \pm$. The right panel shows $j = 1, 2$ bound states. The inset displays the $j = 1$ bound-state energies vs potential depth V_0 for $\lambda = 0.6\Delta$. At some threshold value $V_0 = V_t$ (where $V_t = 0$ for the lowest state shown), a new bound state emerges from the conduction band. This state dives into the valence band for some critical value $V_0 = V_c > V_t$, where the valence band edge is at energy $E_B = E_+ = -0.4\Delta$. For the second bound state in the inset, V_t (V_c) is shown as red (blue) triangle.



141 We always stay within the TI phase $\Delta > \lambda/2$, where bound states are expected for energies $E = E_B$
 142 in the window $\max(\Delta - V_0, E_+) < E_B < \Delta$. For $r < R$, the corresponding radial eigenspinor [see
 143 Eq. (6)] is written with arbitrary prefactors $A_{\pm}^<$ in the form

$$\Phi_j^<(r) = \sum_{\pm} A_{\pm}^< \Phi_{j,\tilde{p}_{\pm}}(r), \quad (23)$$

144 with Eq. (19) for $\Phi_{j,\tilde{p}_{\pm}}(r)$. Here, the $\tilde{p}_{\pm} > 0$ follow from Eq. (18) by including the potential shift,

$$\tilde{p}_{\pm} = (E + V_0 - \Delta)(E + V_0 - E_{\pm}). \quad (24)$$

145 For $r > R$, the general solution is again written as

$$\Phi_j^>(r) = \sum_{\pm} A_{\pm}^> \Phi_{j,p_{\pm}}(r). \quad (25)$$

146 However, now $\Phi_{j,p_{\pm}}$ is given by Eq. (20), since $p_{\pm} < 0$ for true bound states with only evanescent states
 147 outside the potential well.

148 The continuity condition for the four-spinor at the potential step, $\Phi_j^<(R) = \Phi_j^>(R)$, then yields a
 149 homogeneous linear system of equations for the four parameters ($A_{\pm}^<,>$). A nontrivial solution is only
 150 possible when the determinant of the corresponding 4×4 matrix $C(E)$ (which is too lengthy to be given
 151 here but follows directly from the above expressions) vanishes,

$$\det[C(E)] = 0. \quad (26)$$

152 Solving the energy quantization condition (26) then yields the discrete bound-state spectrum (E_B). It is
 153 then straightforward to determine the corresponding spinor wavefunctions.

154 Numerical solution of Eq. (26) yields the bound-state spectrum shown in Fig. 1. When V_0 exceeds a
 155 (j -dependent) ‘‘threshold’’ value, V_t , a bound state splits off the conduction band edge. When increasing
 156 V_0 further, this bound-state energy level moves down almost linearly, cf. inset of Fig. 1, and finally
 157 reaches the valence band edge $E_+ = -\Delta + \lambda$ at some ‘‘critical’’ value $V_0 = V_c$. (For $j = 0$, we will
 158 see below that this definition needs some revision.) Increasing V_0 even further, the bound state is then
 159 expected to dive into the valence band and become a finite-width supercritical resonance, i.e., the energy
 160 would then acquire an imaginary part.

161 3.2. Zero angular momentum states

162 Surprisingly, for $j = 0$, we find a different scenario where supercritical diving, with finite lifetime of
 163 the resonance, happens only for half of the bound states entering the energy window (21). Noting that
 164 states with different parity $\sigma = \pm$ do not mix, see Sec. 2.2, we observe that all $\sigma = +$ bound states enter
 165 the valence band as true bound states (no imaginary part) throughout the energy window (21) while the
 166 valence band continuum is spanned by the $\sigma = -$ states. We then define V_c for ($j = 0, \sigma = +$) bound
 167 states as the true supercritical threshold where $E_B = E_- = -\Delta - \lambda$. However, the ($j = 0, \sigma = -$)
 168 bound states become supercritical already when reaching $E_+ = -\Delta + \lambda$.

169 Therefore an intriguing physical situation arises for $j = 0$ in the energy window (21). While $\sigma = +$
 170 states are true bound states (no lifetime broadening), they coexist with $\sigma = -$ states which span the

171 valence band continuum or possibly form supercritical resonances. For $E < E_-$, however, all bound
 172 states dive, become finite-width resonances, and eventually become dissolved in the continuum.

173 3.3. Threshold for bound states

174 Returning to arbitrary total angular momentum j , we observe that whenever V_0 hits a possible
 175 threshold value V_t , a new bound state is generated, which then dives into the valence band at another
 176 potential depth $V_0 = V_c$ (and so on). Analytical results for all possible threshold values V_t follow by
 177 expanding Eq. (26) for weak dimensionless binding energy $\delta \equiv 1 - E_B/\Delta$. For $\delta \ll 1$ and $j = 1$,
 178 Eq. (26) yields after some algebra

$$\begin{aligned} \delta &= \frac{2(\hbar v_F/R)^2 e^{-2\gamma}}{\Delta^2 \sqrt{1 - \tilde{\lambda}^2}} \left(\frac{1 - \tilde{\lambda}}{1 + \tilde{\lambda}} \right)^{\tilde{\lambda}/2} e^{-\frac{(\hbar v_F/R)^2}{2V_0\Delta} \sum_{\pm} z_{\pm} J_0(z_{\pm})/J_1(z_{\pm})}, \\ z_{\pm} &= \sqrt{V_0(2\Delta \pm \lambda + V_0)}R, \end{aligned} \quad (27)$$

179 where $\gamma \approx 0.577$ is the Euler constant and $\tilde{\lambda} = \lambda/2\Delta$. The binding energy approaches zero for $V_0 \rightarrow 0$,
 180 where Eq. (27) simplifies to

$$\delta = \frac{2(\hbar v_F/R)^2}{\Delta^2 \sqrt{1 - \tilde{\lambda}^2}} \left(\frac{1 - \tilde{\lambda}}{1 + \tilde{\lambda}} \right)^{\tilde{\lambda}/2} e^{-2\gamma - 2\frac{(\hbar v_F/R)^2}{V_0\Delta}}. \quad (28)$$

181 For vanishing Rashba SOI $\lambda = 0$, this reproduces known results [25]. For any $\lambda < 2\Delta$, we observe that
 182 the $j = 1$ bound state in Eq. (28) exists for arbitrarily shallow potential depth V_0 .

183 The threshold values V_t for higher-lying $j = 1$ bound states also follow from the binding energy (27),
 184 since δ vanishes for $J_1(z_+) = 0$ and for $J_1(z_-) = 0$. When one of these two conditions is fulfilled
 185 at some $V_0 = V_t$, a new bound state appears for potential depth above V_t . This statement is in fact
 186 quite general: By similar reasoning, we find that the threshold values V_t for $j = 0$ follow by counting the
 187 zeroes of $J_0(z_{\pm})$. Without SOI, this has also been discussed in [31]. Note that this argument immediately
 188 implies that no bound state with $j = 0$ exists for $V_0 \rightarrow 0$.

189 From the above equations, we can then infer the threshold values V_t for all bound states with $j = 0$
 190 or $j = 1$ in analytical form. These are labeled by $n = 1, 2, \dots$ and $\sigma = \pm$ (for $j = 0$, σ corresponds to
 191 parity),

$$V_{t,j,n,\pm} = (\Delta \pm \lambda/2) \left[-1 + \sqrt{1 + \gamma_{j,n}^2/[R(\Delta \pm \lambda/2)]^2} \right], \quad (29)$$

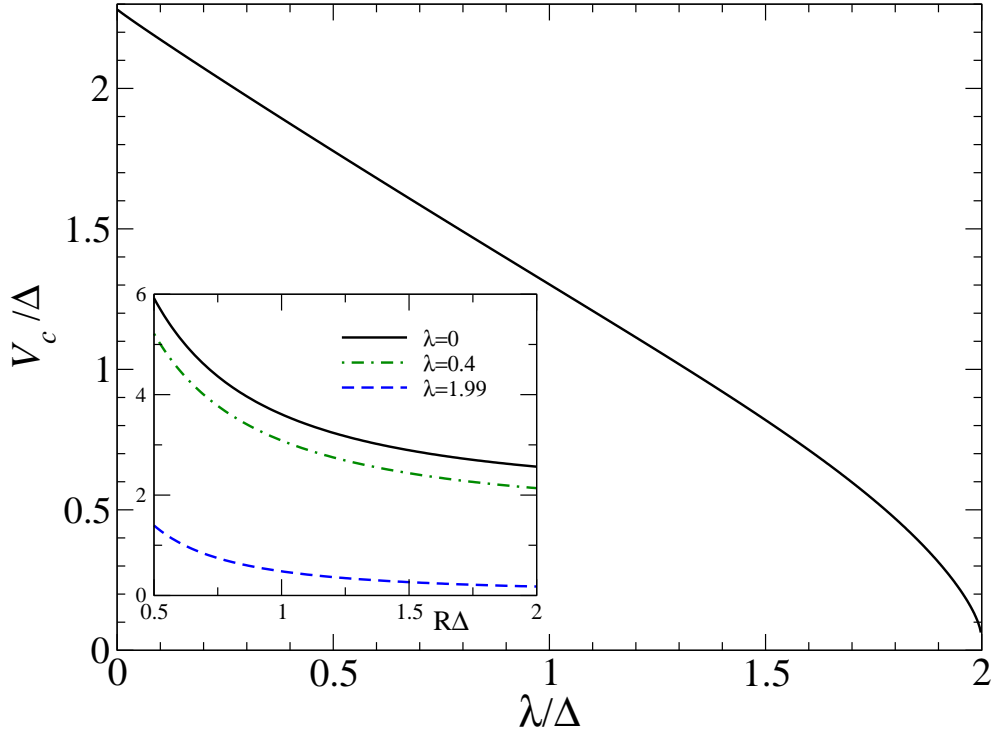
192 where $\gamma_{j,n}$ is the n th zero of the J_j Bessel function.

193 Likewise, for $j > 1$, the condition for the appearance of a new bound state is

$$\sum_{\pm} \left[2(j-1)z_{\pm} J_{j-1}(z_{\pm}) - \frac{(2\Delta \pm \lambda)V_0}{(\hbar v_F/R)^2} J_j(z_{\pm}) \right] J_j(z_{\mp}) = 0. \quad (30)$$

194 Close examination of this condition shows that no bound states with $j > 1$ exist for $V_0 \rightarrow 0$. We
 195 conclude that bound states in a very weak potential well exist only for $j = 1$.

Figure 2. Critical potential depth V_c for the lowest $j = 1$ bound state level in a disk with $R\Delta = 3$. The obtained $\lambda = 0$ value matches the analytical prediction $V_c \approx 2.28\Delta$ from Eq. (31), while $V_c \rightarrow 0$ near the border of the TI phase ($\lambda \rightarrow 2\Delta$). Inset: V_c vs radius R with several values of λ (given in units of Δ) for the lowest bound state.



196 3.4. Supercritical behavior

197 As can be seen in Fig. 1, the lowest $j = 1$ bound state is also the first to enter the valence band
198 continuum for $V_0 = V_c$. For $\lambda = 0$, the critical value is known to be [25]

$$V_c = \Delta \left(1 + \sqrt{1 + \gamma_{0,1}^2 / [R\Delta]^2} \right). \quad (31)$$

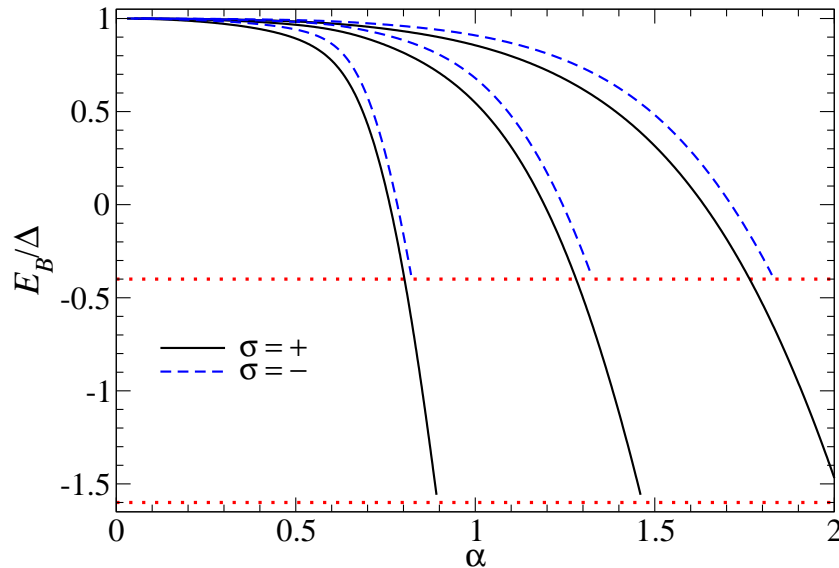
199 with $\gamma_{0,1} \approx 2.41$. The energy of the resonant state acquires an imaginary part for $V_0 > V_c$ [25]. For
200 $\lambda > 0$, we have obtained implicit expressions for V_c , plotted in Fig. 2. Note that these results reproduce
201 Eq. (31) for $\lambda \rightarrow 0$. The almost linear decrease of V_c with increasing λ , see Fig. 2, can be rationalized by
202 noting that the valence band edge is located at $E_+ = -\Delta + \lambda$. Thereby supercritical resonances could be
203 reached already for lower potential depth by increasing the Rashba SOI. Similarly, with increasing disk
204 radius R , the critical value V_c decreases, see the inset of Fig. 2. For the lowest ($j = 0, \sigma = \pm$) bound
205 state, the critical value in fact follows in analytical form,

$$V_{c,\sigma=\pm} = (\Delta \pm \lambda/2) \left(1 + \sqrt{1 + \gamma_{1,1}^2 / [(\Delta \pm \lambda/2)R]^2} \right), \quad (32)$$

206 where $\gamma_{1,1} \approx 3.83$.

207 Since the parity decoupling in Sec. 2.2 only holds for $j = 0$, it is natural to expect that all $j \neq 0$ bound
208 states turn into finite-width resonances when $E_B < E_+$. This expectation is confirmed by an explicit
209 calculation as follows. Within in the window $E_- < E_B < E_+$, a true bound state should not receive
210 a contribution from $\Phi_{j,p+>0}(r)$ for $r > R$, but instead has to be obtained by matching an Ansatz as in

Figure 3. Bound state energies with angular momentum $j = 0$ (E_B in units of Δ) vs dimensionless impurity strength α for the Coulomb problem with regularization parameter $R\Delta = 0.01$ and Rashba SOI $\lambda = 0.6\Delta$. Solid black (dashed blue) curves correspond to parity $\sigma = +$ ($\sigma = -$). Results for radial number $n = 1, 2, 3$ (with increasing energy) are shown. Red dotted lines denote $E = E_{\pm}$.



211 Eq. (23) for the spinor state inside the disk ($r < R$) to an evanescent spinor state $\propto \Phi_{j,p_- < 0}(r > R)$.
 212 However, the matching condition is then found to have no real solution E_B , i.e., there are no true bound
 213 states with $j \neq 0$ in the energy window (21). We therefore conclude that all $j \neq 0$ bound states turn
 214 supercritical when $E_B < E_+$. Note that this statement includes the lowest-lying bound state (which has
 215 $j = 1$). This implies that a finite Rashba SOI can considerably lower the potential depth V_c required for
 216 entering the supercritical regime.

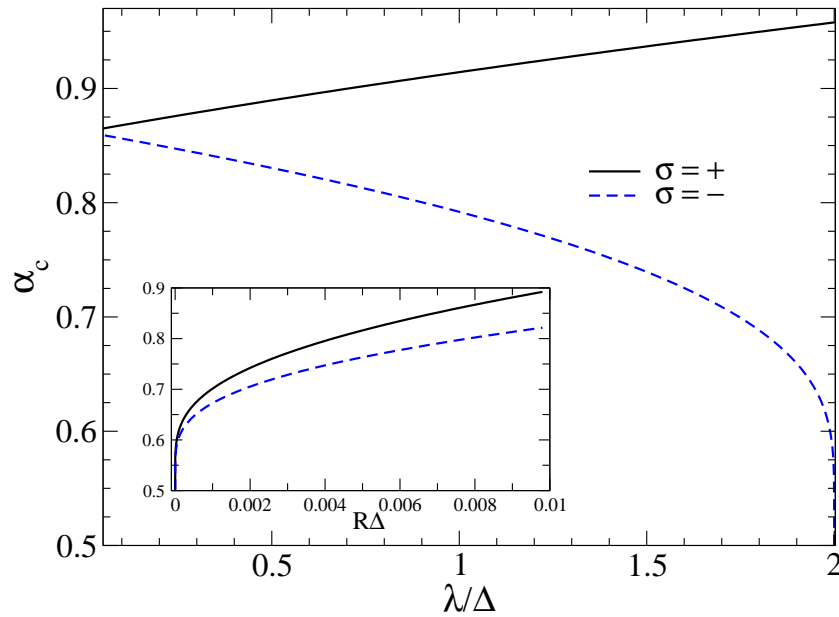
217 4. Coulomb center

218 We now turn to the Coulomb potential, $V(r) = -\alpha/r$, generated by a positively charged impurity
 219 located at the origin, with the dimensionless coupling strength α in Eq. (1). We consider only the TI
 220 phase $\Delta > \lambda/2$ and analyze the bound-state spectrum and conditions for supercriticality. Again, without
 221 loss of generality, we focus on the K point only ($\tau = +$), and first summarize the known solution for
 222 $\lambda = 0$ [2,21,24]. In that case, $s_z = \pm$ is conserved, and the spin-degenerate bound-state energies are
 223 labeled by the integer angular momentum j and a radial quantum number $n = 1, 2, 3, \dots$ (for $j > 0$,
 224 $n = 0$ is also possible),

$$E_{j,n}(\lambda = 0) = \Delta \left(1 + \frac{\alpha^2}{\left(n + \sqrt{(j - 1/2)^2 - \alpha^2} \right)^2} \right)^{-1/2}. \quad (33)$$

225 The corresponding eigenstates then follow in terms of hypergeometric functions. The lowest bound state
 226 is $E_{j=1,n=0} = \Delta\sqrt{1 - 4\alpha^2}$, which dives when $\alpha = \alpha_c = 1/2$; note that α_c precisely corresponds to V_c in
 227 Sec. 3. In particular, for ($j = 0, \sigma = \pm$) states we define α_c in the same manner. Next we discuss how
 228 this picture is modified when the Rashba coupling λ is included.

Figure 4. Main panel: Critical Coulomb impurity strength α_c vs Rashba SOI λ for $R\Delta = 0.01$ and the lowest ($j = 0, \sigma = \pm$) bound states. Inset: α_c vs cutoff scale R for $\lambda = 0.6\Delta$.



229 Following the arguments in Sec. 2.2 for $j = 0$, the combination of Eq. (33) with Eq. (15) immediately
 230 yields the exact bound-state energy spectrum ($n = 1, 2, 3, \dots$),

$$E_{j=0,n,\sigma=\pm} = (\Delta \pm \lambda/2) \left(1 + \frac{\alpha^2}{(n + \sqrt{1/4 - \alpha^2})^2} \right)^{-1/2} \mp \lambda/2. \quad (34)$$

231 The corresponding eigenstates then also follow from Refs. [21,24]. The very same reasoning also applies
 232 to a regularized $1/r$ potential [23,24], where $V(r < R)$ is replaced by the constant value $V = -\alpha/R$.
 233 Here, R is a short-distance cutoff scale of the order of the lattice spacing. The solution of the bound-state
 234 problem then requires a wavefunction matching procedure, which has been carried out in Ref. [24].
 235 Thereby we can already infer all bound states for $j = 0$.

236 Figure 3 shows the resulting $j = 0$ bound-state spectrum vs α for the regularized Coulomb potential.
 237 Within the energy window (21), we again find that states with parity $\sigma = +$ remain true bound states
 238 that dive only for $E_B < E_-$, while $\sigma = -$ states show supercritical diving already for $E_B < E_+$. Figure
 239 4 shows the corresponding critical couplings α_c for $\sigma = \pm$, where the lowest $j = 0$ bound state with
 240 parity σ turns supercritical. Note that for finite R and $\lambda \rightarrow 0$, a unique value for α_c is found, while
 241 for $\lambda \neq 0$ two different critical values for α_c are found. However, this conclusion holds only for finite
 242 regularization parameter R , i.e., it is non-universal. As seen in the inset of Fig. 4, in the limit $R \rightarrow 0$,
 243 both critical values for α_c approach $\alpha_c = 1/2$ again, which is the value found without SOI.

244 Finally, for $j \neq 0$, we can then draw the same qualitative conclusions as in Sec. 3.4 for the potential
 245 well. In particular, we expect that all $j \neq 0$ bound states turn supercritical when their energy E_B reaches
 246 the continuum threshold at $E_B = E_+ = -\Delta + \lambda$.

247 5. Conclusions

248 In this work, we have analyzed the bound-state problem for the Kane-Mele model of graphene with
249 intrinsic (Δ) and Rashba (λ) spin-orbit couplings when a radially symmetric attractive potential $V(r)$ is
250 present. We have focussed on the most interesting “topological insulator” phase with $\Delta > \lambda/2$. The
251 Rashba term λ leads to a restructuring of the valence band, with a halving of the density of states in the
252 window $E_- < E < E_+$, where $E_{\pm} = -\Delta \pm \lambda$. This has spectacular consequences for total angular
253 momentum $j = 0$, where the problem can be decomposed into two independent parity sectors ($\sigma = \pm$).
254 The $\sigma = +$ states remain true bound states even inside the above window and coexist with the continuum
255 solutions as well as possible supercritical resonances in the $\sigma = -$ sector. However, all $j \neq 0$ bound
256 states exhibit supercritical diving for $E < E_+$, where the critical threshold (V_c or α_c for the disk or the
257 Coulomb problem, respectively) is lowered when the Rashba term is present. We hope that these results
258 will soon be put to an experimental test.

259 Acknowledgements

260 This work has been supported by the DFG within the network programs SPP 1459 and SFB-TR 12.

261 References

- 262 1. Castro Neto, A.H.; Guinea, F.; Peres, N.M.R.; Novoselov, K.S.; Geim, A. The electronic properties
263 of graphene. *Rev. Mod. Phys.* **2009**, *81*, 109-162.
- 264 2. Kotov, V.N.; Uchoa, B.; Pereira, V.M.; Guinea, F.; Castro Neto, A.H. Electron-Electron Interactions
265 in Graphene: Current Status and Perspectives. *Rev. Mod. Phys.* **2012**, *84*, 1067-1125.
- 266 3. Kane, C.L.; Mele, E.J. Quantum Spin Hall Effect in Graphene. *Phys. Rev. Lett.* **2005**, *95*, 226801.
- 267 4. Hasan, M.Z.; Kane, C.L. Topological Insulators. *Rev. Mod. Phys.* **2010**, *82*, 3045-3067.
- 268 5. Huertas-Hernando, D.; Guinea, F.; Brataas, A. Spin-orbit coupling in curved graphene, fullerenes,
269 nanotubes, and nanotube caps. *Phys. Rev. B* **2006**, *74*, 155426.
- 270 6. Min, H.; Hill, J.E.; Sinitsyn, N.A.; Sahu, B.R.; Kleinman, L.; MacDonald, A.H. Intrinsic and Rashba
271 spin-orbit interactions in graphene sheets. *Phys. Rev. B* **2006**, *74*, 165310.
- 272 7. Yao, Y.; Ye, F.; Qi, X.L.; Zhang, S.C.; Fang, Z. Spin-orbit gap of graphene: First-principles
273 calculations. *Phys. Rev. B* **2007**, *75*, 041401(R).
- 274 8. Weeks, C.; Hu, J.; Alicea, J.; Franz, M.; Wu, R. Engineering a Robust Quantum Spin Hall State in
275 Graphene via Adatom Deposition. *Phys. Rev. X* **2011**, *1*, 021001.
- 276 9. Shevtsov, O.; Carmier, P.; Groth, C.; Waintal, X.; Carpentier, D. Graphene-Based Heterojunction
277 between Two Topological Insulators. *Phys. Rev. X* **2012**, *2*, 031004.
- 278 10. Shevtsov, O.; Carmier, P.; Groth, C.; Waintal, X.; Carpentier, D. Tunable thermopower in a
279 graphene-based topological insulator. *Phys. Rev. B* **2012**, *85*, 245441.
- 280 11. Jiang, H.; Qiao, Z.; Liu, H.; Shi, J.; Niu, Q. Stabilizing topological phases in graphene via random
281 adsorption. *Phys. Rev. Lett.* **2012**, *109*, 116803.
- 282 12. Bercioux, D.; De Martino, A. Spin-resolved scattering through spin-orbit nanostructures in
283 graphene. *Phys. Rev. B* **2010**, *81*, 165410.
- 284 13. Lenz, L.; Bercioux, D. Dirac-Weyl electrons in a periodic spin-orbit potential. *EPL* **2011**, *96*,
285 27006.

- 286 14. Wang, Y.; Brar, V.W.; Shytov, A.V.; Wu, Q.; Regan, W.; Tsai, H.Z.; Zettl, A.; Levitov, L.S.;
287 Crommie, M.F. Mapping Dirac quasiparticles near a single Coulomb impurity on graphene. *Nature*
288 *Physics* **2012**, *8*, 653.
- 289 15. Katsnelson, M.I. Nonlinear screening of charge impurities in graphene. *Phys. Rev. B* **2006**, *74*,
290 201401(R).
- 291 16. Pereira, V.M.; Nilsson, J.; Castro Neto, A.H. Coulomb Impurity Problem in Graphene. *Phys. Rev.*
292 *Lett.* **2007**, *99*, 166802.
- 293 17. Shytov, A.V.; Katsnelson, M.I.; Levitov, L.S. Vacuum Polarization and Screening of Supercritical
294 Impurities in Graphene. *Phys. Rev. Lett.* **2007**, *99*, 236801.
- 295 18. Shytov, A.V.; Katsnelson, M.I.; Levitov, L.S. Atomic Collapse and Quasi-Rydberg states in
296 Graphene. *Phys. Rev. Lett.* **2007**, *99*, 246802.
- 297 19. Biswas, R.R.; Sachdev, S.; Son, D.T. Coulomb impurity in graphene. *Phys. Rev. B* **2007**, *76*,
298 205122.
- 299 20. Fogler, M.M.; Novikov, D.S.; Shklovskii, B.I. Screening of hypercritical charge in graphene. *Phys.*
300 *Rev. B* **2007**, *76*, 233402.
- 301 21. Novikov, D.S. Elastic scattering theory and transport in graphene. *Phys. Rev. B* **2007**, *76*, 245435.
- 302 22. Terekhov, I.S.; Milstein, A.I.; Kotov, V.I.; Sushkov, O.P. Screening of Coulomb impurities in
303 graphene. *Phys. Rev. Lett.* **2008**, *100*, 076803.
- 304 23. Pereira, V.M.; Kotov, V.N.; Castro Neto, A.H. Supercritical Coulomb impurities in gapped
305 graphene. *Phys. Rev. B* **2008**, *78*, 085101.
- 306 24. Gamayun, O.B.; Gorbar, E.V.; Gusynin, V.P. Supercritical Coulomb center and excitonic instability
307 in graphene. *Phys. Rev. B* **2009**, *80*, 165429.
- 308 25. Gamayun, O.B.; Gorbar, E.V.; Gusynin, V.P. Magnetic field driven instability of a charged center in
309 graphene. *Phys. Rev. B* **2011**, *83*, 235104.
- 310 26. Zhu, J.L.; Sun, S.; Yang, N. Dirac donor states controlled by magnetic field in gapless and gapped
311 graphene. *Phys. Rev. B* **2012**, *85*, 035429.
- 312 27. Huertas-Hernando, D.; Guinea, F.; Brataas, A. Spin-Orbit Mediated Spin Relaxation in Graphene.
313 *Phys. Rev. Lett.* **2009**, *103*, 146801.
- 314 28. Rashba, E.I. Graphene with structure-induced spin-orbit coupling: Spin-polarized states, spin zero
315 modes, and quantum Hall effect. *Phys. Rev. B* **2009**, *79*, 161409(R).
- 316 29. De Martino, A.; Hütten, A.; Egger, R. Landau levels, edge states, and strained magnetic waveguides
317 in graphene monolayers with enhanced spin-orbit interaction. *Phys. Rev. B* **2011**, *84*, 155420.
- 318 30. Rakyta, P.; Kormanyos, A.; Cserti, J. Trigonal warping and anisotropic band splitting in monolayer
319 graphene due to Rashba spin-orbit coupling. *Phys. Rev. B* **2010**, *82*, 113405.
- 320 31. Bardarson, J.H.; Titov, M.; Brouwer, P.W. Electrostatic confinement of electrons in an integrable
321 graphene quantum dot. *Phys. Rev. Lett.* **2009**, *102*, 226803.